Supercritical CO₂ produces the visible-light-responsive TiO₂/COF heterojunction with enhanced electron-hole separation for high-performance hydrogen evolution

Lifei Liu[1,2], Jianling Zhang[1,2,3] (✉), Xiuniang Tan[1,2], Bingxing Zhang[1,2], Jinbiao Shi[1,2], Xiuyan Cheng[1,2], Dongxing Tan[1,2], Buxing Han[1,2,3], Lirong Zheng[4], and Fanyu Zhang[1,2]

[1] Beijing National Laboratory for Molecular Sciences, CAS Key Laboratory of Colloid, Interface and Chemical Thermodynamics, CAS Research/Education Center for Excellence in Molecular Sciences, Institute of Chemistry, Chinese Academy of Sciences, Beijing 100190, China
[2] School of Chemical Sciences, University of Chinese Academy of Sciences, Beijing 100049, China
[3] Physical Science Laboratory, Huairou National Comprehensive Science Center, Beijing 101400, China
[4] Beijing Synchrotron Radiation Facility (BSRF), Institute of High Energy Physics, Chinese Academy of Sciences, Beijing 100049, China

ABSTRACT

To construct the heterojunctions of TiO₂ with other compounds is of great importance for overcoming its inherent shortages and improving the visible-light photocatalytic performance. Here we propose the construction of TiO₂/covalent organic framework (COF) heterojunction with tight connection by a supercritical CO₂ (SC CO₂) method, which helps bridging the transformation paths for photo-induced charge between TiO₂ and COF. The produced TiO₂/COF heterojunction performs a H₂ evolution of 3,962 μmol·g^{-1}·h^{-1} under visible-light irradiation, which is ~ 25 times higher than that of pure TiO₂ and 4.5 folds higher than that of TiO₂/COF synthesized by the conventional solvothermal method. This study opens up new possibilities for constructing heterojunctions for solar energy utilization.

KEYWORDS

supercritical CO₂, covalent organic framework (COF), TiO₂, H₂ production, visible light

1   Introduction

Since the first report of titanium dioxide (TiO₂) for photo-electrocatalytic H₂ production in 1972 by Fujishima and Honda [1, 2], the direct conversion of solar energy to hydrogen energy becomes possible. TiO₂ has been extensively researched in the past decades for its non-toxicity, abundance, low cost, chemical stability and ultra-high activity [3, 4]. However, limited by the low quantum efficiency and wide band gap (3.0–3.2 eV), TiO₂ is photo-reactive only in ultra-violate (UV) region below 380 nm [5]. Thus the utilization of visible light which accounts for 43% in the total solar power remains to be developed [6, 7]. So far, considerable efforts have been devoted to narrow the band gap and enhance the visible-light absorption of TiO₂, including heteroatom doping [8, 9], metal deposition [10–13] and introducing heterojunction [14–16]. Among these methods, the construction of heterojunction structures of TiO₂ with semiconductors [17, 18], polymers [19, 20], carbon nanotubes [21, 22] etc. has attracted much interest. In general, the heterojunctions are produced by solvothermal method, which usually causes the relatively loose connection between the two compounds and thus restricts their photoelectrical properties for catalysis. It is desirable to develop TiO₂ heterojunctions combined by strong interactions for further improved electron-hole separation efficiency as well as visible-light absorption.

Being one of the most abundant green solvents on the earth, supercritical CO₂ (SC CO₂) has aroused much attention for its unique features such as the low viscosity and surface tension; high solubility, diffusivity and penetrability [23, 24]. Here, we demonstrate for the first time a SC CO₂-assisted route for the construction of TiO₂/COF heterojunction with tight connection (Scheme 1). The utilization of SC CO₂ combines many advantages. First, SC CO₂ favors the Ti-N bond formation of TiO₂/COF heterojunction, which improves the electron-hole separation efficiency. Second, the small and uniform TiO₂ nanoparticles are well dispersed on the shell of COF spheres owing to the facilitated diffusion and penetration of TiO₂ precursor across COF shell assisted by SC CO₂ [25]. Moreover, the combination of TiO₂ and COF causes a broader absorbance in visible-light region. Owing to these unique features, the as-synthesized TiO₂/COF heterojunction exhibits greatly improved H₂ evolution under visible-light irradiation compared with pure TiO₂.

2   Experimental

2.1   Materials

Tetrabutyl titanate (TBT) (purity ≥ 98.5%) was purchased from Beijing Xingjin Chemical Factory. Benzidine (Bd) (purity ≥ 98.0%) was supported by Aladdin Industrial Corporation.

1,3,5-triformylbenzene (Tb) (purity 96%) was provided by Beijing InnoChem Science & Technology Co., Ltd. Triethanolamine (TEOA) (purity > 99%) was purchased from Acros Organics, USA. $H_2PtCl_6 \cdot 6H_2O$ (purity 99.9%) was supported by J&K Scientific Ltd. Deionized water, dimethyl formamide (DMF), tetrahydrofuran, ethyl alcohol (EtOH), acetic acid and dioxane were purchased from Beijing Chemical Works. Nafion D-521 dispersion (5% w/w in water and 1-propanol, ≥ 0.92 meq/g exchange capacity) was provided by Alfa Aesar China Co., Ltd. N_2 (purity 99.999%) and CO_2 (purity 99.999%) were purchased from Beijing Analysis Instrument Factory.

2.2 Synthesis of TbBd

A 50 mL stainless steel vessel was charged with Tb (147 mg, 0.9 mmol) and dioxane (5 mL). The mixture was sonicated for 10 min to get a homogeneous dispersion. Afterwards, Bd (249 mg, 1.35 mmol) in 5 mL of dioxane solution was added, and the resultant suspension was briefly sonicated for 1 min. Subsequently, acetic acid (3 M, 1.8 mL) was added and the vessel was then sealed and left undisturbed for 3 d at 120 °C. The precipitate was collected by centrifugation and washed with DMF and anhydrous tetrahydrofuran separately. The collected powder was then activated by solvent exchange with anhydrous methanol for 3 times and dried at 80 °C under vacuum for 12 h to give a yellow powder with 80% isolated yield and a molecular formula of $(C_{126}H_{86}N_{12})_n$.

2.3 Preparation of TiO₂/TbBd-1

In a typical experiment, 50 mg of TbBd, 50 mg TBT was dispersed in 5 mL EtOH. After a brief sonication of 1 min, the resultant suspension was transferred to a 15 mL Teflon-lined stainless steel vessel. 200 μL water was injected in the pipeline of the vessel in advance. As CO_2 was pumped into the vessel, the pre-injected water was rushed into the vessel at the same time. After the desired pressure (5.52 MPa) had been reached under thermal equilibrium (25 °C) controlled by a water bath, the vessel was transferred in an oil bath at 120 °C for 24 h reaction. Then CO_2 was removed by depressurization. The precipitate was collected by centrifugation and washed with EtOH and dried at 80 °C under vacuum for 12 h to give a yellow powder.

2.4 Preparation of TiO₂/TbBd-2

TiO_2/TbBd-2 was synthesized in the same conditions with that of TiO_2/TbBd-1, except that CO_2 was not charged into the reaction system.

2.5 Synthesis of TiO₂

TiO_2 was synthesized in the same conditions with that of TiO_2/TbBd-1, except that TbBd was not added into the reaction system.

2.6 Characterizations

X-ray diffraction (XRD) was performed using a Rigaku D/max-2500 diffractometer with Cu Kα radiation (λ = 1.5418 Å) at 40 kV and 200 mA. The morphology of catalyst was characterized by scanning electron microscope (SEM) (HITACHI S-4800) and transmission electron microscope (TEM) (JEM-1011). The X-ray photoelectron spectroscopy (XPS) was performed using a multipurpose X-ray photoemission spectroscope (Thermo Scientific ESCALAB 250Xi). The contents of Ti in composites were determined by inductively coupled plasma atomic emission spectroscopy (ICP-AES) (VISTA-MPX). The Xenon lamp (300 W) was provided by Zhongjiaojinyuan Co., Ltd. The optical absorption property was characterized by

ultraviolet visible diffused reflectance spectrum (UV–vis DRS, UV-2600, SHIMADZU). The XAFS experiment was carried out at Beamline 1W1B at Beijing Synchrotron Radiation Facility (BSRF). Data of X-ray absorption fine structure (XAFS) were processed using the Athena program of thee IFEFFIT package based on FEFF 6. Prior to merging, spectra were aligned to the first and largest peak in the smoothed first derivative of the absorption spectrum, background removed, and spectra processed to obtain a normalized unit edge step. Data were processed with k^3-weighting and a Rbkg value of 1.0. Merged data sets were aligned to the largest peak in the first derivative of the adsorption spectrum. Normalized $\mu(E)$ data were obtained directly from the Athena program of the IFEFFIT package.

2.7 Photocatalytic H₂ generation

In a typical experiment, 10 mg of photocatalyst was pre-dispersed in the mixture of water/TEOA (9 mL/1 mL) in a round-bottom flask (100 mL). Then 30 μL of H_2PtCl_6 aqueous solution (10 mg·mL^{-1}) was added to deposit 3% Pt nanoparticles as co-catalysts by a photodeposition method. The system was vacuum-treated several times and bubbled with N_2 for 30 min to remove the dissolved air. Artificial visible light (wavelength range, 380 nm ≤ λ ≤ 780 nm) was supplied by a 300 W Xenon lamp to start the photoreaction. The water bath was used to maintain the temperature at 25 °C. After reaction for 4 h, the produced H_2 was analyzed by gas chromatograph (GC, HP 4890D), which was equipped with FID and TCD detectors using helium as internal standard.

2.8 Photoelectrochemical properties

Transient photocurrents measurements were conducted in a three-electrode system, in which the samples were uniformly coated on a FTO substrate (1.05 cm ×1.25 cm), serving as the working electrodes. Besides, a Pt wire and an Ag/AgCl electrode served as the count and reference electrodes, respectively. 0.2 M Na_2SO_4 aqueous solution was employed as electrolyte. The illumination source adopted in photocurrent ON/OFF cycles was the same with that in photocatalytic H_2 generation. Transient photocurrents and EIS Nyquist plots were measured on the same electrochemical workstation (CHI660E).

3 Results and discussion

The scheme for the synthesis of TiO_2/TbBd is illustrated in Scheme 1 (see experimental details in the Electronic Supplementary Material (ESM)). Firstly, the COF hollow spheres of TbBd was synthesized from Tb and Bd by a solvothermal route. Afterwards, TbBd was dispersed in EtOH containing a certain amount of TBT, followed by pumping compressed CO_2 into the reactor with a small amount of water (5.52 MPa). The system was heated to 120 °C and kept for 12 h. The hybrid material prepared was denoted as TiO_2/TbBd-1.

The TbBd shows hollow spheres with diameter of 526 ± 90 nm and wall thickness of 68 ± 25 nm, as characterized by SEM and TEM (Figs. 1(a)–1(c) and Fig. S1 in the ESM). For TiO_2/TbBd-1, the hollow sphere structure of TbBd is well kept (Figs. 1(d)–1(f)). However, the wall thickness of TiO_2/TbBd-1 doubles approximately (141 ± 22 nm) as compared with that of TbBd. It can be attributed to both the swelling effect of COF shells by SC CO_2 [26] and the incorporation of TiO_2 nanoparticles on the surface of TbBd hollow sphere. From the magnified TEM image (Fig. 1(f)), it is evident that the TiO_2 nanoparticles with particle size of 5.6 ± 1.2 nm are uniformly incorporated on the hollow sphere of TbBd. The high-resolution TEM (HRTEM) image shows three lattice spacings of 3.51, 2.39 and 1.90 Å (Fig. 1(g)),
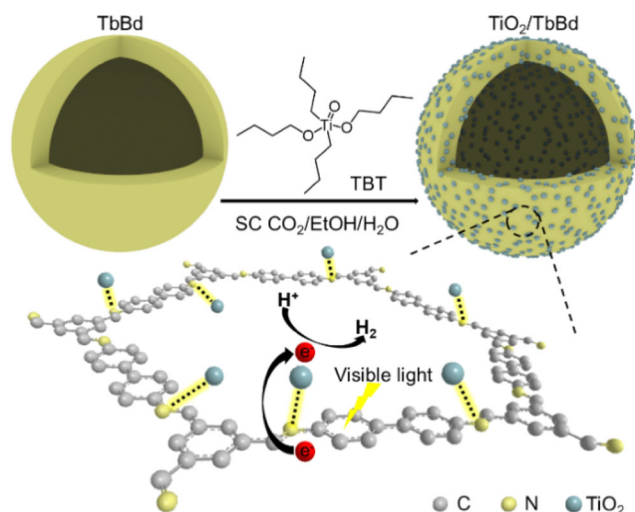
Scheme 1 Schematic illustration of the synthesis of TiO₂/TbBd hybrid material and the transformation paths (Ti–N bonds) of photo-excited electrons during visible-light catalysis.

corresponding to the characteristic lattice planes for (101), (004) and (200) of anatase TiO_2, respectively [27]. Energy-dispersive X-ray (EDX) element mapping images reveal that Ti, O, N and C elements distribute uniformly on the hollow spheres of TbBd (Fig. 1(h)), indicating the even distribution of TiO_2 nanoparticles on TbBd. The content of TiO_2 in TiO₂/TbBd-1 was determined to be 16.5 wt.% by ICP-AES analysis. For the XRD pattern of TiO₂/TbBd-1 (Fig. 1(i), and Fig. S2 in the ESM), the intense peak at 3.54° corresponds to the (100) plane of TbBd [28, 29], which is in good agreement with the featured mesopores of TbBd (2.6 nm) in diameter [28]. The diffractions at 25.32°, 37.68° and 47.96° correspond to the characteristic lattice planes of (101), (004) and (200) of anatase TiO_2, respectively, which is consistent with the lattice spacings measured by HRTEM (Fig. 1(g)). All the diffractions of TiO₂/TbBd-1 show good agreement with the corresponding simulated XRD patterns of TbBd and anatase TiO_2, demonstrating the formation of TbBd

and TiO_2 hybrid with structural integrity. The TiO₂/TbBd-1 has a Brunauer-Emmett-Teller (BET) surface area of 162.5 $m^2 \cdot g^{-1}$, which is lower than that of TbBd (638.0 $m^2 \cdot g^{-1}$), as determined by N_2 adsorption-desorption measurement (Fig. S3 in the ESM). It is consistent with the loading of TiO_2 nanoparticles on TbBd, which can occupy or block the internal pores of TbBd.

For comparison, the control sample TiO₂/TbBd-2 was prepared without the addition of SC CO_2, while the other experimental conditions were the same with those for synthesizing TiO₂/TbBd-1. XRD proves the formation of anatase TiO₂/TbBd hybrid material (Fig. 1(i)). TEM images reveal severe aggregation of TiO_2 nanoparticles in TiO₂/TbBd-2 (Fig. S4 in the ESM). It indicates that SC CO_2 plays a critical role in producing the highly dispersed and uniform TiO_2 nanoparticles on TbBd.

The interactions between TiO_2 and TbBd in TiO₂/TbBd-1 and TiO₂/TbBd-2 were studied by Fourier transform infrared (FT-IR) spectra. As can be seen from the curve I of Fig. 2(a), the TiO₂/TbBd-1 shows characteristic absorptions resulting from TiO_2 and TbBd, indicating the formation of TiO₂/TbBd-1 composite. For example, the broad absorption ranging from 400 to 850 cm^{-1} corresponds to the bridging stretching mode of Ti–O–Ti and the stretching vibration of Ti–O, the vibration absorption of C=N at 1,622 cm^{-1} is characteristic of the formation of TbBd from the condensation of aldehyde and amine groups, and the absorptions in the range from 1,450 to 1,600 cm^{-1} correspond to the skeleton vibration of aromatic ring [28]. Remarkably, the Ti–O–Ti stretching peak of TiO₂/TbBd-1 is observed at 601.8 cm^{-1} (Fig. S5 in the ESM), far more higher than that of pure TiO_2 (curve III, 563.2 cm^{-1}). It can be ascribed to the formation of O–Ti–N and N–Ti–N bonds [30, 31], indicating the strong interactions between TiO_2 and TbBd in TiO₂/TbBd-1. In a contrast, the TiO₂/TbBd-2 shows the absorption at a wavenumber (curve II, 561.3 cm^{-1}) similar with that of TiO_2 (563.2 cm^{-1}), suggesting there exists negligible interactions between TiO_2 and TbBd in TiO₂/TbBd-2. The results above prove that SC CO_2 plays a key role in the formation of O–Ti–N and N–Ti–N bonds during the synthesis process for TiO₂/TbBd heterojunction.
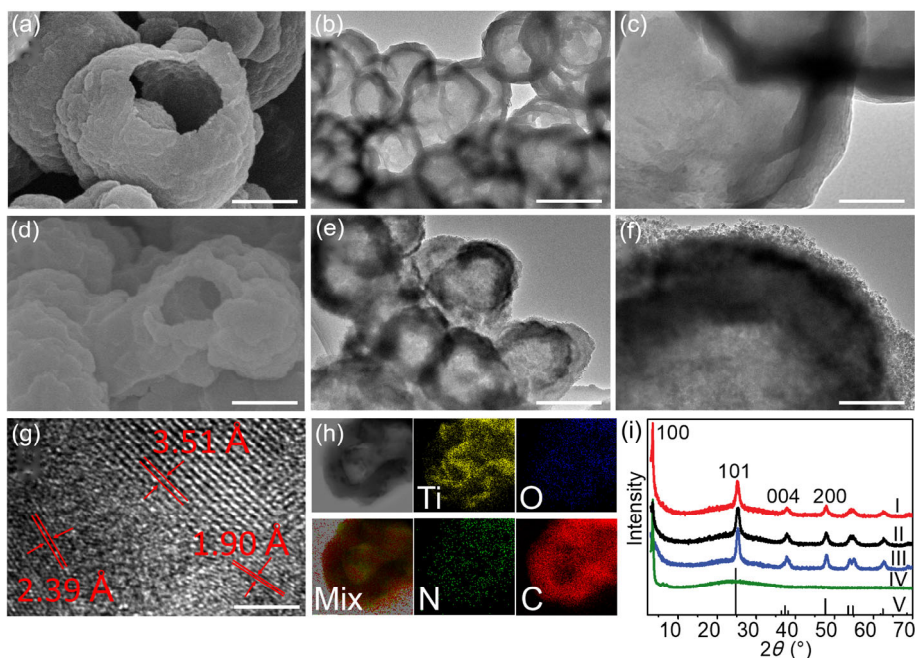

Figure 1 SEM (a) and TEM ((b) and (c)) images of TbBd; SEM (d), TEM ((e) and (f)), HRTEM (g) images and EDX elemental mapping (h) of TiO₂/TbBd-1; XRD patterns (i) of TiO₂/TbBd-1 (I), TiO₂/TbBd-2 (II), TiO₂ (III), TbBd (IV) and the simulated XRD pattern of anatase TiO₂ (V). Scale bars: 150 nm in ((a) and (d)), 500 nm in ((b) and (e)), 100 nm in ((c) and (f)), and 3 nm in (g).
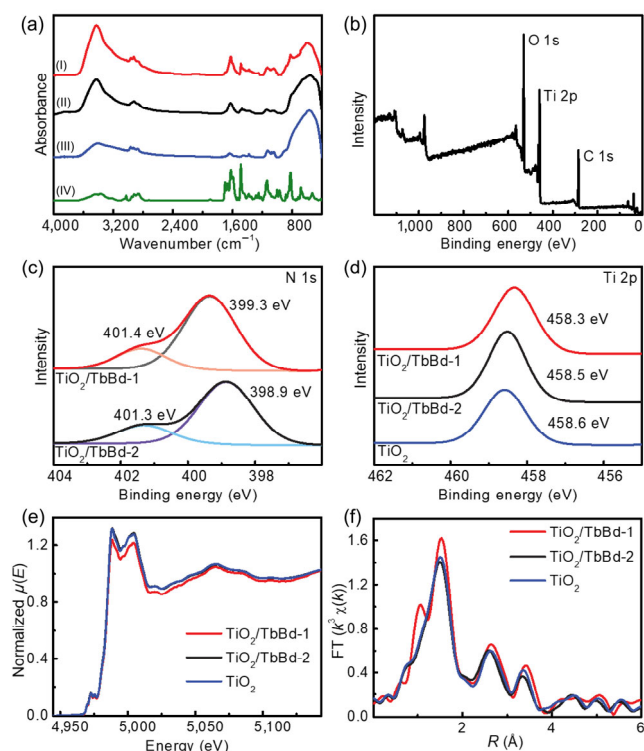
Figure 2 (a) FT-IR spectra of TiO₂/TbBd-1 (I), TiO₂/TbBd-2 (II), TiO₂ (III) and TbBd (IV). (b) XPS spectrum of TiO₂/TbBd-1. N 1s (c) and Ti 2p (d) XPS spectra for TiO₂/TbBd-1, TiO₂/TbBd-2 and TiO₂. XANES (e) and EXAFS (f) spectra of TiO₂/TbBd-1, TiO₂/TbBd-2 and TiO₂ at Ti K-edge.

XPS was further employed to investigate the surface composition and bond state of TiO₂/TbBd-1 and TiO₂/TbBd-2. The obvious peaks of C, O and Ti can be detected in the wide XPS scanning spectra of TiO₂/TbBd-1 (Fig. 2(b)) and TiO₂/TbBd-2 (Fig. S6 in the ESM). Two typical peaks are shown in fitted N 1s high-resolution XPS spectra of TiO₂/TbBd-1 and TiO₂/TbBd-2 (Fig. 2(c)), including N=C (401.4 and 401.3 eV) and N–C (399.3 and 398.9 eV) [32]. For TiO₂/TbBd-1, the N 1s binding energy of N–C (399.3 eV) is 0.4 eV greater than that of TiO₂/TbBd-2 (398.9 eV). This binding energy shift is due to the formation of specific Ti–N bonds and the improved 1s electron binding energy of N atom in the environment of O–Ti–N. The Ti 2p high-resolution XPS spectra of TiO₂/TbBd-1, TiO₂/TbBd-2 and TiO₂ are shown in Fig. 2(d). In comparison to TiO₂ (458.6 eV), the Ti 2p binding energy of TiO₂/TbBd-1 (458.3 eV) exhibits a decrease of 0.3 eV, corresponding to the formation of Ti–N bonds [30]. As a contrast, the Ti 2p binding energy of TiO₂/TbBd-2 (458.5 eV) is similar with that of TiO₂ (458.6 eV), suggesting the maintained structure of TiO₂. The results above give further support for the key role of SC CO₂ in assisting the formation of Ti–N bonds in TiO₂/TbBd-1.

The local structure of TiO₂/TbBd-1 was studied by synchrotron X-ray absorption spectra (XAS), as well as those of TiO₂/TbBd-2 and TiO₂. As shown in the Ti *K*-edge X-ray absorption near-edge structure (XANES) spectra (Fig. 2(e)), the absorption edge intensity of TiO₂/TbBd-1 decreases obviously compared with TiO₂ and TiO₂/TbBd-2, suggesting the valence state of Ti in TiO₂/TbBd-1 is lower than Ti(IV) [33]. The Fourier-transformed Ti *K*-edge extended X-ray absorption fine-structure (EXAFS) spectra for all samples show two intense peaks centered near 1.53 and 2.64 Å (Fig. 2(f)), which correspond to the first- and second-shell distances within the crystalline TiO₂. The first peak arises from the first neighbors of oxygen or nitrogen around Ti, representing the Ti–O or Ti–N bond length. The second corresponds to Ti···Ti distances in

the surrounding central Ti [34]. TiO₂/TbBd-1 shows higher *R* value (1.53 Å) of the first coordination shell compared with those of TiO₂/TbBd-2 (1.50 Å) and TiO₂ (1.50 Å). It further proves that there is strong interactions between TiO₂ and TbBd in TiO₂/TbBd-1.

The above results show that SC CO₂ plays a critical role in producing the highly dispersed and uniform TiO₂ nanoparticles on TbBd. It can be attributed to the low viscosity, zero surface tension and high penetrability of SC CO₂ [35, 36], which facilitate the immobilization and dispersion of the precursor of TiO₂ (TBT) on TbBd. Therefore, the highly dispersed, uniform and small TiO₂ nanoparticles are formed on TbBd with the assist of SC CO₂. The as-produced small TiO₂ nanoparticles have high surface area and oxygen vacancies. The unsaturated titanium on the surface of TiO₂ nanoparticle can bond with the nitrogen on TbBd to form a TiO₂-TbBd heterojunction. Such a TiO₂/COF heterojunction with tight connection by SC CO₂-assisted route is expected to exhibit improved optoelectronic properties for photocatalysis.

The light absorption, utilization and transformation of TiO₂/TbBd-1 were determined. As shown in the UV–vis DRS, TiO₂/TbBd-1 well inherits the optical features of both TiO₂ and TbBd (Fig. 3(a)). Compared with TiO₂, the absorption edge of TiO₂/TbBd-1 is largely expanded to visible-light region below 500 nm. Such a greatly enhanced visible-light absorption ability is favorable for the visible-light photocatalysis [37, 38]. The corresponding band gaps for TbBd and TiO₂ were calculated to be 2.61 and 3.37 eV, respectively (Figs. S7 and S8 in the ESM). The Mott-Schottky measurements indicate that the flat band position (V_{fb}) of TbBd and TiO₂ are −0.75 and −0.50 V vs. normal hydrogen electrode (NHE) (Fig. 3(b) and Fig. S9 in the ESM), respectively. Combined with the band gaps calculated above, the valence band (VB) positions of TbBd and TiO₂ are +1.86 and +2.87 V vs. NHE. These results show that the TiO₂/TbBd-1 belongs to type II heterojunction [39].

The photocatalytic performance of TiO₂/TbBd-1 for water splitting was investigated with artificial visible-light irradiation (see experimental details in the ESM). A typical time course of H₂ evolution as catalyzed by TiO₂/TbBd-1 is shown in Fig. 4(a). For comparison, the photocatalytic performances of TiO₂/TbBd-2 and TiO₂ for water splitting were also determined. The H₂ production of TiO₂/TbBd-1 exhibits a total amount of 81 μmol H₂ at reaction time of 12 h, much higher than that of TiO₂/TbBd-2 (20 μmol) and TiO₂ (16 μmol). Under the same reaction conditions, no H₂ was detected without either irradiation or photocatalyst, which indicate that the generation of H₂ is from the photocatalytic system. Moreover, no photocatalytic activity was detected by pure TbBd. Thus, the evolution efficiency of H₂ is presented by turn over frequency (TOF, μmol·g⁻¹·h⁻¹) based on the content of TiO₂. The TOF values of the three catalysts are shown in Fig. 4(b). TiO₂/TbBd-1 displays a photocatalytic H₂ evolution rate of 3,962 μmol·g⁻¹·h⁻¹, nearly 25 and 4.5 times higher than those of TiO₂ (154 μmol·g⁻¹·h⁻¹) and TiO₂/TbBd-2 (710 μmol·g⁻¹·h⁻¹), respectively. As compared with the reported TiO₂-based catalysts, TiO₂/TbBd-1 is among
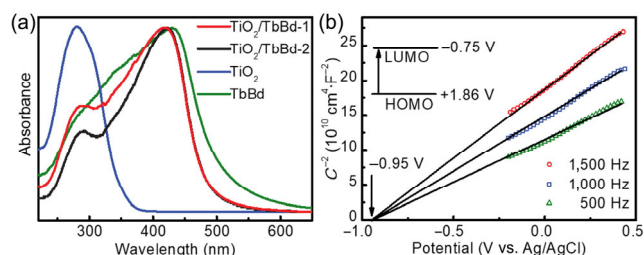

Figure 3 (a) UV–vis DRS spectra of TiO₂/TbBd-1, TiO₂/TbBd-2, TiO₂ and TbBd. (b) Mott-Schottky plots and band energy (inset) for TbBd.
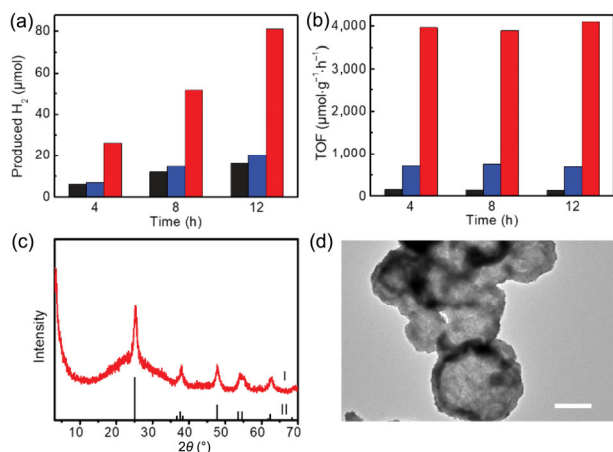
Figure 4 Time course of H_2 evolution (a) and TOF values (b) of TiO$_2$/TbBd-1 (red), TiO$_2$/TbBd-2 (blue) and TiO$_2$ (black) varied with reaction time. (c) XRD pattern of TiO$_2$/TbBd-1 after 12 h photocatalysis (I) and the simulated XRD pattern of anatase TiO$_2$ (II). (d) TEM image of TiO$_2$/TbBd-1 after 12 h photocatalysis. Scale bar: 500 nm. Reaction conditions: 10 mg catalyst, 9 mL H_2O, 1 mL TEOA, simulated visible light (380 nm $\leq \lambda \leq$ 780 nm) irradiation with a 300 W xenon lamp.

the best for photocatalytic H_2 production (Table S1 in the ESM). There is no decrease tendency of the photocatalytic activity with prolonged reaction time, indicating the stability of TiO$_2$/TbBd-1. The TiO$_2$/TbBd-1 well keeps the crystallinity and morphology after photocatalytic H_2 production for 12 h (Figs. 4(c) and 4(d)).

The results above reveal that the TiO$_2$/TbBd-1 prepared with the assistance of SC CO$_2$ exhibits extremely high photocatalytic activity for H_2 production. The underlying mechanism was studied. Electrochemical impedance spectroscopy (EIS) measurement was conducted to explore the internal resistance in the charge transfer process of the samples (Fig. 5(a)). TiO$_2$/TbBd-1 displays the smallest semicircular diameter of Nyquist curves compared with TiO$_2$/TbBd-2, TiO$_2$ and TbBd, demonstrating the smallest interfacial resistance of charge transfer [40]. The photocurrent density of TiO$_2$/TbBd-1 is about 2 times higher than that of TiO$_2$/TbBd-2 (Fig. 5(b)). It further indicates the better separation of photogenerated charges of TiO$_2$/TbBd-1. The enhanced charge-separation efficiency is confirmed by photoluminescence (PL) emission spectra (Fig. 5(c)) [25]. The PL intensity of TiO$_2$/TbBd-1 is significantly
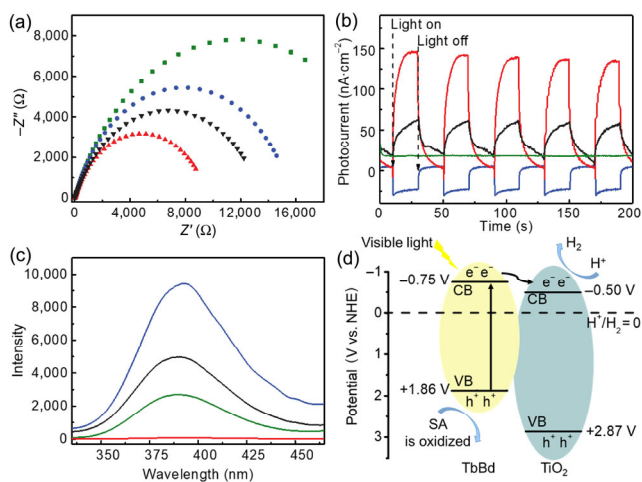
quenched in comparison with that of the parent TbBd and TiO$_2$. In contrast, TiO$_2$/TbBd-2 shows a moderate intensity between TbBd and TiO$_2$. The more quenched PL intensity of TiO$_2$/TbBd-1 compared with TiO$_2$/TbBd-2 suggests that the separation efficiency of photogenerated charges is effectively improved by the construction of heterojunction with the assistance of SC CO$_2$.

Based on the above results, a schematic illustration of the transfer and separation of photogenerated charges in TiO$_2$/TbBd-1 is proposed (Fig. 5(d)). The conduction band (CB) levels are co-related with photocatalytic efficiencies stated above. TbBd with excellent visible-light absorbance serves as solar energy absorber. As excited by visible light, the photogenerated electrons migrate from VB to CB, and further transfer to the CB of TiO$_2$ through Ti–N bonds, which serve as the transformation paths of photo-excited electrons in TiO$_2$/TbBd heterojunction. The separated electrons in CB of TiO$_2$ participate in the reduction of H^+, and the holes left in VB of TbBd are reduced by sacrifice agent. The separation of photogenerated electrons and holes can efficiently prolong the lifetime of charge carriers and hinder the charge recombination, thus promoting the solar energy conversion [41, 42].

4   Conclusion

In conclusion, we propose the SC CO$_2$-assisted construction of TiO$_2$/COF heterojunction, which successfully narrows the band gap of the hybrid material and thus accelerates the transformation of photoelectrons from COF to TiO$_2$. The H_2 evolution is highly improved, ~ 25 times higher than that of pure TiO$_2$ and 4.5 folds higher than that of TiO$_2$/COF made from the conventional solvothermal method. This work opens up a new route for constructing TiO$_2$/COF heterojunctions by supercritical fluid, through which the transformation paths for photo-induced charge can be successfully bridged for highly improved H_2 evolution. We anticipate that more heterojunctions with different compositions and properties can be fabricated by this method in future for highly efficient solar energy utilization.

Electronic Supplementary Material: Supplementary material (schematic, TEM images, N$_2$ adsorption-desorption isotherms, XPS spectrum, band gap energy and Mott-Schottky plots) is available in the online version of this article at https://doi.org/10.1007/s12274-020-2728-6.

Figure 5   (a) EIS Nyquist plots. (b) Transient photocurrents measurements. (c) PL spectra with the excitation wavelength of 240 nm for TiO$_2$/TbBd-1 (red), TiO$_2$/TbBd-2 (black), TiO$_2$ (blue) and TbBd (green). (d) Schematic illustration for the charge transfer and separation in the SC CO$_2$-assisted TiO$_2$/TbBd hybrid material under visible-light irradiation.

References

[1] Fujishima, A.; Zhang, X. T.; Tryk, D. A. TiO$_2$ photocatalysis and related surface phenomena. *Surf. Sci. Rep.* **2008**, *63*, 515−582.

[2] Fujishima, A.; Honda, K. Electrochemical photolysis of water at a semiconductor electrode. *Nature* **1972**, *238*, 37−38.

[3] Ola, O.; Maroto-Valer, M. M. Review of material design and reactor engineering on TiO$_2$ photocatalysis for CO$_2$ reduction. *J. Photochem. Photobiol. C: Photochem. Rev.* **2015**, *24*, 16−42.

[4] Low, J.; Cheng, B.; Yu, J. G. Surface modification and enhanced photocatalytic CO$_2$ reduction performance of TiO$_2$: A review. *Appl. Surf. Sci.* **2017**, *392*, 658−686.

[5] Etacheri, V.; Di Valentin, C.; Schneider, J.; Bahnemann, D.; Pillai, S. C. Visible-light activation of TiO₂ photocatalysts: Advances in theory and experiments. *J. Photochem. Photobiol. C: Photochem. Rev.* **2015**, *25*, 1−29.

[6] Asahi, R.; Morikawa, T.; Ohwaki, T.; Aoki, K.; Taga. Y. Visible-light photocatalysis in nitrogen-doped titanium oxides. *Science* **2001**, *293*, 269−271.

[7] Ni, M.; Leung, M. K. H.; Leung, D. Y. C.; Sumathy, K. A review and recent developments in photocatalytic water-splitting using TiO₂ for hydrogen production. *Renew. Sustain. Energy Rev.* **2007**, *11*, 401−425.

[8] Zhang, Z. G.; Huang, Z. F.; Cheng, X. D.; Wang, Q. L.; Chen, Y.; Dong, P. M.; Zhang, X. W. Product selectivity of visible-light photocatalytic reduction of carbon dioxide using titanium dioxide doped by different nitrogen-sources. *Appl. Surf. Sci.* **2015**, *355*, 45−51.

[9] Zhang, Q. Y.; Li, Y.; Ackerman, E. A.; Gajdardziska-Josifovska, M.; Li, H. L. Visible light responsive iodine-doped TiO₂ for photocatalytic reduction of CO₂ to fuels. *Appl. Catal. A: Gen.* **2011**, *400*, 195−202.

[10] Tian, H.; Zhang, X. L.; Scott, J.; Ng, C.; Amal, R. TiO₂-supported copper nanoparticles prepared via ion exchange for photocatalytic hydrogen production. *J. Mater. Chem. A* **2014**, *2*, 6432−6438.

[11] Wang, E. J.; Yang, W. S.; Cao, Y. A. Unique surface chemical species on indium doped TiO₂ and their effect on the visible light photocatalytic activity. *J. Phys. Chem. C* **2009**, *113*, 20912−20917.

[12] Feng, X. J.; Sloppy, J. D.; LaTempa, T. J.; Paulose, M.; Komarneni, S.; Bao, N. Z.; Grimes, C. A. Synthesis and deposition of ultrafine Pt nanoparticles within high aspect ratio TiO₂ nanotube arrays: Application to the photocatalytic reduction of carbon dioxide. *J. Mater. Chem.* **2011**, *21*, 13429−13433.

[13] Hou, W. B.; Hung, W. H.; Pavaskar, P.; Goeppert, A.; Aykol, M.; Cronin, S. B. Photocatalytic conversion of CO₂ to hydrocarbon fuels via plasmon-enhanced absorption and metallic interband transitions. *ACS Catal.* **2011**, *1*, 929−936.

[14] Yu, J. G.; Wang, S. H.; Low, J.; Xiao, W. Enhanced photocatalytic performance of direct Z-scheme g-C₃N₄-TiO₂ photocatalysts for the decomposition of formaldehyde in air. *Phys. Chem. Chem. Phys.* **2013**, *15*, 16883−16890.

[15] Yan, H. J.; Yang, H. X. TiO₂-g-C₃N₄ composite materials for photocatalytic H₂ evolution under visible light irradiation. *J. Alloys Compd.* **2011**, *509*, L26−L29.

[16] Chen, Y. F.; Huang, W. X.; He, D. L.; Situ, Y.; Huang, H. Construction of heterostructured g-C₃N₄/Ag/TiO₂ microspheres with enhanced photocatalysis performance under visible-light irradiation. *ACS Appl. Mater. Interfaces* **2014**, *6*, 14405−14414.

[17] Zheng, L. X.; Han, S. C.; Liu, H.; Yu, P. P.; Fang, X. S. Hierarchical MoS₂ nanosheet@TiO₂ nanotube array composites with enhanced photocatalytic and photocurrent performances. *Small* **2016**, *12*, 1527−1536.

[18] Li, H. F.; Yu, H. T.; Quan, X.; Chen, S.; Zhao, H. M. Improved photocatalytic performance of heterojunction by controlling the contact facet: High electron transfer capacity between TiO₂ and the {110} facet of BiVO₄ caused by suitable energy band alignment. *Adv. Funct. Mater.* **2015**, *25*, 3074−3080.

[19] Hao, R. R.; Wang, G. H.; Tang, H.; Sun, L. L.; Xu, C.; Han, D. Y. Template-free preparation of macro/mesoporous g-C₃N₄/TiO₂ heterojunction photocatalysts with enhanced visible light photocatalytic activity. *Appl. Catal. B: Environ.* **2016**, *187*, 47−58.

[20] Hou, H. J.; Zhang, X. H.; Huang, D. K.; Ding, X.; Wang, S. Y.; Yang, X. L.; Li, S. Q.; Xiang, Y. G.; Chen, H. Conjugated microporous poly(benzothiadiazole)/TiO₂ heterojunction for visible-light-driven H₂ production and pollutant removal. *Appl. Catal. B: Environ.* **2017**, *203*, 563−571.

[21] Luo, Q.; Ma, H.; Zhang, Y.; Yin, X. W.; Yao, Z. B.; Wang, N.; Li, J. B.; Fan, S. S.; Jiang, K. L.; Lin, H. Cross-stacked superaligned carbon nanotube electrodes for efficient hole conductor-free perovskite solar cells. *J. Mater. Chem. A* **2016**, *4*, 5569−5577.

[22] Akhavan, O.; Abdolahad, M.; Abdi, Y.; Mohajerzadeh, S. Synthesis of titania/carbon nanotube heterojunction arrays for photoinactivation of *E. coli* in visible light irradiation. *Carbon* **2009**, *47*, 3280−3287.

[23] DeSimone, J. M.; Guan, Z.; Elsbernd, C. S. Synthesis of fluoropolymers in supercritical carbon dioxide. *Science* **1992**, *257*, 945−947.

[24] Hasell, T.; Parker, D. J.; Jones, H. A.; McAllister, T.; Howdle, S. M. Porous inverse vulcanised polymers for mercury capture. *Chem. Commun.* **2016**, *52*, 5383−5386.

[25] Zhang, F. M.; Sheng, J. L.; Yang, Z. D.; Sun, X. J.; Tang, H. L.; Lu, M.; Dong, H.; Shen, F. C.; Liu, J.; Lan, Y. Q. Rational design of MOF/COF hybrid materials for photocatalytic H₂ evolution in the presence of sacrificial electron donors. *Angew. Chem., Int. Ed.* **2018**, *57*, 12106−12110.

[26] Üzer, S.; Akman, U.; Hortacsu, Ö. Polymer swelling and impregnation using supercritical CO₂: A model-component study towards producing controlled-release drugs. *J. Supercrit. Fluids* **2006**, *38*, 119−128.

[27] Zhang, W.; He, H. L.; Tian, Y.; Lan, K.; Liu, Q.; Wang, C. Y.; Liu, Y.; Elzatahry, A.; Che, R. C.; Li, W. et al. Synthesis of uniform ordered mesoporous TiO₂ microspheres with controllable phase junctions for efficient solar water splitting. *Chem. Sci.* **2019**, *10*, 1664−1670.

[28] Gao, C. H.; Lin, G.; Lei, Z. X.; Zheng, Q.; Lin, J. S.; Lin, Z. A. Facile synthesis of core-shell structured magnetic covalent organic framework composite nanospheres for selective enrichment of peptides with simultaneous exclusion of proteins. *J. Mater. Chem. B* **2017**, *5*, 7496−7503.

[29] Vitaku, E.; Dichtel, W. R. Synthesis of 2D imine-linked covalent organic frameworks through formal transimination reactions. *J. Am. Chem. Soc.* **2017**, *139*, 12911−12914.

[30] Etacheri, V.; Seery, M. K.; Hinder, S. J.; Pillai, S. C. Highly visible light active TiO₂₋ₓNₓ heterojunction photocatalysts. *Chem. Mater.* **2010**, *22*, 3843−3853.

[31] Patrahau, B.; Chaumont, C.; Barloy, L.; Hellwig, P.; Henry, M.; Melin, F.; Pauly, M.; Mobian, P. From a bulk solid to thin films of a hybrid material derived from the [Ti₁₀O₁₂(cat)₈(py)₈] oxo-cluster and poly(4-vinylpyridine). *New J. Chem.* **2019**, *43*, 1581−1588.

[32] Mu, X. W.; Zhan, J.; Feng, X. M.; Yuan, B. H.; Qiu, S. L.; Song, L.; Hu, Y. Novel melamine/o-phthalaldehyde covalent organic frameworks nanosheets: Enhancement flame retardant and mechanical performances of thermoplastic polyurethanes. *ACS Appl. Mater. Interfaces* **2017**, *9*, 23017−23026.

[33] Bolis, V.; Bordiga, S.; Lamberti, C.; Zecchina, A.; Carati, A.; Rivetti, F.; Spanò, G.; Petrini, G. A calorimetric, IR, XANES and EXAFS study of the adsorption of NH₃ on Ti-silicalite as a function of the sample pre-treatment. *Microporous Mesoporous Mater.* **1999**, *30*, 67−76.

[34] Farges, F. A Ti K-edge EXAFS study of the medium range environment around Ti in oxide glasses. *J. Non-Cryst. Solids* **1999**, *244*, 25−33.

[35] Reverchon, E. Supercritical fluid extraction and fractionation of essential oils and related products. *J. Supercrit. Fluids* **1997**, *10*, 1−37.

[36] Zu, G. Q.; Shen, J.; Zou, L. P.; Wang, F.; Wang, X. D.; Zhang, Y. W.; Yao, X. D. Nanocellulose-derived highly porous carbon aerogels for supercapacitors. *Carbon* **2016**, *99*, 203−211.

[37] Liu, H.; Huang, B. L.; Zhou, J. H.; Wang, K.; Yu, Y. S.; Yang, W. W.; Guo, S. J. Enhanced electron transfer and light absorption on imino polymer capped PdAg nanowire networks for efficient room-temperature dehydrogenation of formic acid. *J. Mater. Chem. A* **2018**, *6*, 1979−1984.

[38] Gao, M. Y.; Yu, Y. S.; Yang, W. W.; Li, J.; Xu, S. C.; Feng, M.; Li, H. B. Ni nanoparticles supported on graphitic carbon nitride as visible light catalysts for hydrolytic dehydrogenation of ammonia borane. *Nanoscale* **2019**, *11*, 3506−3513.

[39] Gholipour, M. R.; Dinh, C. T.; Béland, F.; Do, T. O. Nanocomposite heterojunctions as sunlight-driven photocatalysts for hydrogen production from water splitting. *Nanoscale* **2015**, *7*, 8187−8208.

[40] Guo, X.; Li, M. G.; Liu, Y. Q.; Huang, Y. R.; Geng, S.; Yang, W. W.; Yu, Y. S. Hierarchical core-shell electrode with NiWO₄ nanoparticles wrapped MnCo₂O₄ nanowire arrays on Ni foam for high-performance asymmetric supercapacitors. *J. Colloid Interface Sci.* **2020**, *563*, 405−413.

[41] Schneider, J.; Matsuoka, M.; Takeuchi, M.; Zhang, J. L.; Horiuchi, Y.; Anpo, M.; Bahnemann, D. W. Understanding TiO₂ photocatalysis: Mechanisms and materials. *Chem. Rev.* **2014**, *114*, 9919−9986.

[42] Liu, H.; Liu, X. Y.; Yang, W. W.; Shen, M. Q.; Geng, S.; Yu, C.; Shen, B.; Yu, Y. S. Photocatalytic dehydrogenation of formic acid promoted by a superior PdAg@g-C₃N₄ Mott–Schottky heterojunction. *J. Mater. Chem. A* **2019**, *7*, 2022−2026.